SOFT ROBOTS

High-performance electrified hydrogel actuators based on wrinkled nanomembrane electrodes for untethered insect-scale soft aquabots

Jongkuk Ko[1], Changhwan Kim[2], Dongjin Kim[2], Yongkwon Song[1], Seokmin Lee[1], Bongjun Yeom[3], June Huh[1,4], Seungyong Han[2], Daeshik Kang[2], Je-Sung Koh[2]*, Jinhan Cho[1,5]*

Hydrogels have diverse chemical properties and can exhibit reversibly large mechanical deformations in response to external stimuli; these characteristics suggest that hydrogels are promising materials for soft robots. However, reported actuators based on hydrogels generally suffer from slow response speed and/or poor controllability due to intrinsic material limitations and electrode fabrication technologies. Here, we report a hydrogel actuator that operates at low voltages (<3 volts) with high performance (strain > 50%, energy density > 7×10^5 joules per cubic meter, and power density > 3×10^4 watts per cubic meter), surpassing existing hydrogel actuators and other types of electroactive soft actuators. The enhanced performance of our actuator is due to the formation of wrinkled nanomembrane electrodes that exhibit high conductivity and excellent mechanical deformation through capillary-assisted assembly of metal nanoparticles and deswelling-induced wrinkled structures. By applying an electric potential through the wrinkled nanomembrane electrodes that sandwich the hydrogel, we were able to trigger a reversible and substantial electroosmotic water flow inside a hydrogel film, which drove the controlled swelling of the hydrogel. The high energy efficiency and power density of our wrinkled nanomembrane electrode–induced actuator enabled the fabrication of an untethered insect-scale aquabot integrated with an on-board control unit demonstrating maneuverability with fast locomotion speed (1.02 body length per second), which occupies only 2% of the total mass of the robot.

INTRODUCTION

Rapid technological progress in microprocessors, energy storage, and electromechanical devices has strongly stimulated the successful development of electrified insect-scale (or milliscale) soft robots (*1*–*6*) exhibiting various locomotive motions in unexpected complex environments. Although there have been notable advances in electric vehicles and robots based on conventional electric motors and electromechanical actuators, technological advances in miniaturized electronic applications have progressed relatively slowly because of the fundamental limitations of conventional electric motors with rigid/bulky components that exhibit poor performance on a small scale. To resolve these critical drawbacks, research efforts have been devoted to developing electroactive soft actuators that emulate various compliant motions shown in biological organisms. However, many challenging attempts at integrating electroactive soft actuators with electronic components have faced a notable trade-off between the weight/size and energy/power density of soft actuators as well as between the electrical conductivity and mechanical deformation of actuator electrodes because of limited actuation performances and strict operating conditions. Consequently, reported electroactive soft actuators have generally needed a bulky, tethered power supply, which has restricted the range of their applicability (*1*–*8*). Specifically, state-of-the-art untethered soft aquabots driven by dielectric elastomer actuators (*9*–*11*), ionic polymer-metal composite actuators (*12*, *13*), and others (*14*, *15*) must be constructed with a relatively large body size (>7 cm) and tethered external power supply because of their high operating voltages (about a few kilovolts) and/or poor actuation performances. Therefore, electroactive soft actuators operating at low voltage/power with a high degree of portability and performance are highly desirable for next-generation robotics based on soft materials.

Hydrogels represent an exciting class of responsive soft matter, which allow various chemical modifications and the ability to generate mechanical deformations and forces by osmotic pressure–induced water diffusion in response to small changes in stimuli, such as heat (*16*–*19*), light (*19*–*21*), chemicals (*22*, *23*), pH (*24*), and humidity (*25*, *26*), thereby providing distinct advantages over other types of responsive soft matter requiring relatively large external stimuli. However, because of the intrinsically slow nature of water diffusion within the hydrogel matrix, the abovementioned environmental stimuli–responsive hydrogels have suffered from slow response speed and poor controllability, which seriously limit practical applications. Therefore, the construction of autonomous/mobile robotic systems with soft hydrogel–based actuators remains a major challenge.

As an alternative, the application of electric potential on hydrogels (or ionic gel) with embedded ionic components can provide an effective way to accelerate and control reversible water diffusion, which can notably enhance the response speed and controllability of actuators. Among these electrically actuating mechanisms, electroosmosis directly generates a dragging force on bulk fluids within the hydrogel matrix by establishing electric field–induced electric

[1]Department of Chemical and Biological Engineering, Korea University, 145 Anam-ro, Seongbuk-gu, Seoul 02841, Republic of Korea. [2]Department of Mechanical Engineering, Ajou University, 206 Worldcup-ro, Yeongtong-gu, Suwon 16499, Republic of Korea. [3]Department of Chemical Engineering, Hanyang University, Seongdong-gu, Seoul 04763, Republic of Korea. [4]Department of Life Sciences, Korea University, Seoul 02841, Republic of Korea. [5]KU-KIST Graduate School of Converging Science and Technology, Korea University, 145 Anam-ro, Seongbuk-gu, Seoul 02841, Republic of Korea.
*Corresponding author. Email: jinhan71@korea.ac.kr (J.C.); jskoh@ajou.ac.kr (J.-S.K.)

double layers in the hydrogel, which provides a more efficient hydraulic fluid flow process than other mechanisms (particularly electrothermal or electrochemical mechanisms). In particular, electroosmosis and electrically triggered osmosis have recently shown great promise to overcome the intrinsic limitations of hydrogels including diffusion-limited water transport. Specifically, it has been reported that hydrogel actuators with turgor (*27*) or bistable (*28*) design can exhibit high actuation forces or instantaneously enhanced actuation speed, respectively. However, they still have issues with slow actuation speed (about a few minutes) and bulky/rigid actuation setup as well as relatively high operating voltages (>5 to 10 V) due to the use of conventional conductive materials and electrode designs.

Despite the benefits of the electroosmosis mechanism, reported electrode fabrication approaches have restricted further advancement of hydrogel actuators because of unfavorable interfacial interactions between hydrogels and conductive components. Specifically, hydrogel-based electrodes have been mainly prepared via simple approaches such as coating (*29*–*37*) and embedding (*38*–*41*) of conductive components. The resulting hydrogel electrodes have exhibited considerably low electrical conductivity with slightly increased mechanical deformability (*37*, *38*) [e.g., 4310 S cm^{-1} with <10% stretchability for the coating method (*37*) and 377 S cm^{-1} with 250% stretchability for the embedding method (*38*)], in sharp contrast to previously reported dried elastomer-based electrodes (*42*–*45*). As a result, almost all electroactive hydrogel actuators reported to date can be operated by externally positioned electrodes (*27*, *28*, *46*, *47*) or bulky electrodes poorly bonded to hydrogels (*14*, *17*, *31*, *33*) exhibiting limited electrical conductivity and deformability. Thus, it is expected that the development of hydrogel electrodes with high electrical conductivity (even under large mechanical deformation) combined with a hydrogel with desirable chemical/mechanical properties will make an important breakthrough in the area of electroactive hydrogel actuators.

Here, we introduce an electroactive hydrogel actuator based on wrinkled nanomembrane electrodes (WNEs) that is driven by electroosmosis (WNE-hydrogel actuators) (Fig. 1A). We also highlight that our approach resolves the drawbacks (i.e., slow response speed, poor controllability, high operation voltage, and low energy/power density) of previously reported soft actuators, including electric stimuli–induced hydrogel actuators. For this study, an assembly approach, called "capillary-assisted in situ assembly of metal nanoparticles," was newly developed for preparation of WNE-hydrogel actuators. The proposed approach induces vertical and lateral growth of densely packed metal nanoparticle (NP) arrays on wet hydrogel surfaces through continuous capillary transport and ligand exchange reactions of amine-functionalized polymer linkers within hydrogels in a nonpolar medium. After the formation of these robust metal NP layers on the hydrogel surface, subsequent deswelling of the hydrogel in a nonpolar medium generates a WNE that can simultaneously realize high electrical conductivity (4.1×10^4 S cm^{-1}) and high mechanical deformability (110% stretchability), which stands in contrast to conventional hydrogel electrodes (*29*–*41*). In addition to metal NP assembly, the hydrogel body was chemically modified for enhanced Young's modulus, optimal swelling degree/rate, and controlled fraction of ionic groups and could be successfully used as an ionic liquid reservoir and a porous membrane for electroosmosis as well as an actuating body for swelling/deswelling.

Because of the unique operation mechanism and the electrode structure shown in our study, the WNE-hydrogel actuators displayed high actuation performance (i.e., an actuation strain of >50%, an energy density of $>7 \times 10^5$ J m^{-3}, and a power density of $>3 \times 10^4$ W m^{-3}) with low operation voltage (<3 V) and power consumption (<40 mW cm^{-2}). Although previously reported electrochemically driven actuators (e.g., ionic polymer metal composite and carboneous electrode-ionic polymer composite) can also be operated at relatively low voltage (<3 V), their performance has been intrinsically restricted because of the fundamental limitations of their working mechanisms (i.e., electrochemical reactions and/or electrostatic repulsion concentrically occurring on the surface of the electrodes) and the mechanically stiff electrode layer. To further demonstrate the high performance of WNE-hydrogel actuators, we designed one of the smallest and fast-moving untethered soft aquabot among the various aquabots reported to date, mimicking natural propulsion motion (Fig. 1B). In particular, note that the WNE actuator occupied only 2% of the total body mass of the robot, which could not be realized with conventional electric motors or soft actuators (*9*–*15*). Considering the high performance, we believe that our approach provides a basis for developing and designing a variety of high-performance soft actuator–based applications, including biomedical devices, micromanipulators, and other types of autonomous milliscale robots.

RESULTS

Preparation of WNEs on hydrogels

To fabricate the WNE-hydrogel actuators based on the capillary-assisted in situ metal NP assembly (Fig. 1), we first immersed a copolymerized poly(acrylic acid)-poly(acrylamide) (PAA-*co*-PAAm) hydrogel (fig. S1) in poly(ethylenimine) (PEI) aqueous solution (pH 11) for infiltration of PEI into the hydrogel. In particular, note that the monomer types and compositions of PAA-*co*-PAAm (8:2) hydrogels used in our study were determined from preliminary experimental results related to swelling ratio, electroosmosis, and actuation performance (fig. S2). In this case, a large amount of carboxylic acid (COOH) groups of PAA-*co*-PAAm hydrogels in the pH 11 PEI solution [pK_a (where K_a is the acid dissociation constant) of PEI, ~10] were converted to carboxylate ion (COO^-) groups (pK_a of PAA, ~4.5), which caused the hydrogels to swell by more than a factor of 10 (in volume) due to strong electrostatic repulsions between negatively charged COO^- groups. More specifically, the swelling ratio of the hydrogel was increased from 1 to 11.4 with increases in the PEI concentration from 0 to 30 mg ml^{-1} (fig. S3). In this case, the infiltrated PEI served as an additional cross-linker within the hydrogel via mixed interactions (i.e., hydrogen bonding and electrostatic interaction) between the NH_2/partial NH_3^+ groups of PEI and the partial COOH/COO^- groups of hydrogels, which also had a notable effect on the mechanical stiffness of the hydrogels. That is, when using a PEI solution (30 mg ml^{-1}), the Young's modulus of the hydrogel was increased up to 4.2 MPa, which was about 14 times higher than that (0.3 MPa) of a hydrogel immersed in a PEI solution (1 mg ml^{-1}) (fig. S3). This facile control of mechanical stiffness is highly beneficial for achieving high performance in hydrogel actuators, because their performance is closely related to the swelling ratio and mechanical stiffness of the

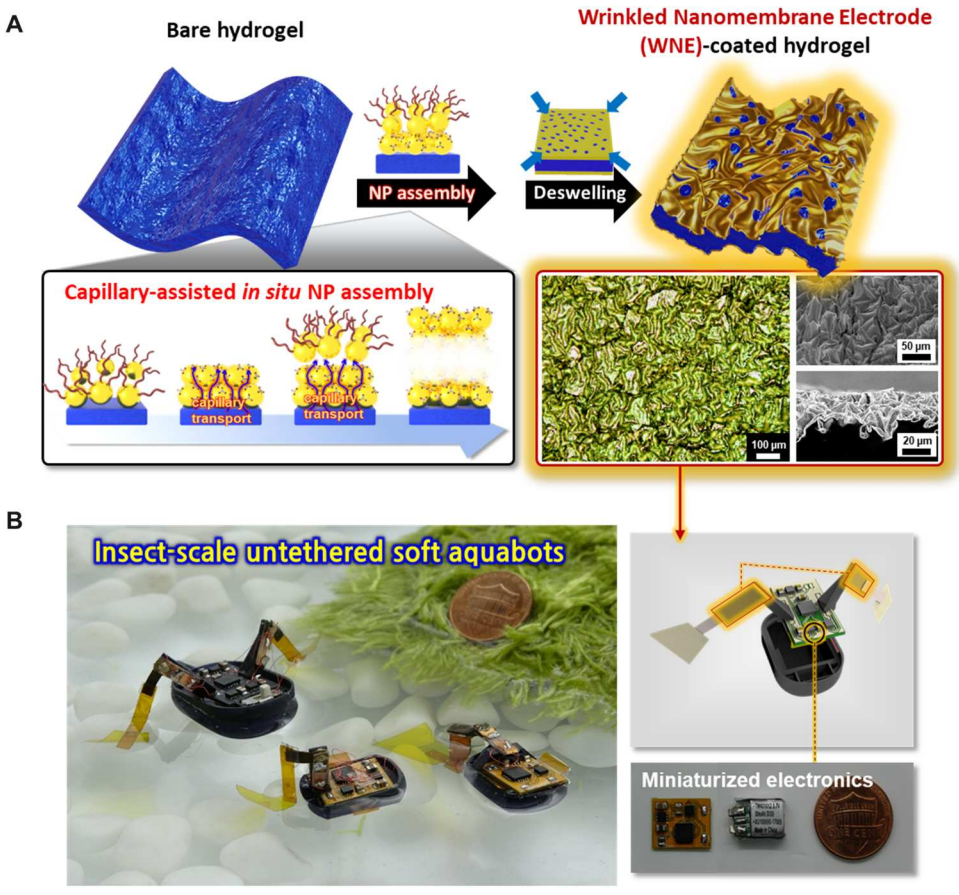

Fig. 1. Insect-scale untethered soft aquabots by WNE-coated hydrogel actuators. (**A**) Schematic illustration of the formation of WNEs prepared from capillary-assisted in situ NP assembly and deswelling processes with their consequent optical microscopy and SEM images. (**B**) Schematic illustration and photographic image of the representative untethered soft aquabots integrated with WNE-hydrogel actuator, circuit board, and battery.

hydrogel. On the basis of these results, the concentration of the PEI solution used in preparing hydrogel bodies was fixed at 30 mg ml^{-1}. Considering that the swelling degree and Young's modulus are two conflicting mechanical properties of hydrogel, note that enhancing their properties at the same time is quite challenging.

The swollen PEI-infiltrated hydrogel was subsequently dipped into a toluene solution containing tetraoctylammonium-stabilized Au NPs (TOA-Au NPs) with diameters of about 8 nm (fig. S4), followed by both the formation of dense Au NP layers onto hydrogel and the deswelling (49% reduction compared with the initial PEI-infiltrated hydrogel) of the resultant Au NP–coated hydrogel (Fig. 2A). With increasing deposition time for the TOA-Au NPs, the adsorbed Au NPs were converted to porous Au nanomembrane films composed of numerous Au nanoplates, which caused an increase in the thickness of the Au nanomembrane [from 32 nm (for 30 min) to 125 nm (for 3 hours)] and an increase in lateral size (figs. S5 and S6). This unique phenomenon was mainly due to the primary amine (NH_2) groups of the infiltrated PEI, which have a higher binding affinity for the Au NP surface than the ammonium groups of native TOA ligands. That is, TOA ligands loosely bound to the surfaces of Au NPs were replaced by NH_2-functionalized PEI at the interface between the aqueous and toluene solutions, resulting in room-temperature sintering of adjacent Au NPs without the repetitive ligand exchange processes used in the layer-by-layer assembly approach (*48*, *49*). It has been recently reported that sufficiently small interparticle distance (<5 Å) can induce metallic bonding between adjacent metal NPs with low cohesive energy through reciprocal atom diffusion, which enables notable sintering at room temperature (*50*). The role of the PEI on the sintering of Au NPs was investigated by analyzing the conformations of PEI adsorbed between adjacent Au NPs using molecular dynamics (MD) simulations (fig. S7). The simulation results showed that PEI chains sandwiched between Au surfaces adopted flat conformations to maximize the number of PEI atoms within a radius of van der Waals interactions with Au atoms, indicating more favorable interactions between PEI and Au surface than intra- or intermolecular PEI interactions. The minimal separation (by sandwiched PEI monolayer) between neighboring Au surfaces was estimated to be about 5.6 Å. Although the calculated separation gap was slightly larger than the threshold distance (~5 Å) for the metallic sintering between neighboring Au NPs (*48*–*50*), it could sufficiently give rise to the Au NP sintering by small structural fluctuations (possibly due to the fluctuation-induced transient exposure of bare Au NP surface). Therefore, continuous capillary transport of PEI from the inside of the hydrogel to the outermost nanoporous NP layers could accelerate formation of Au nanoplates and porous Au nanomembranes through vertical and lateral growth of Au NPs at the water/toluene interface (fig. S5).

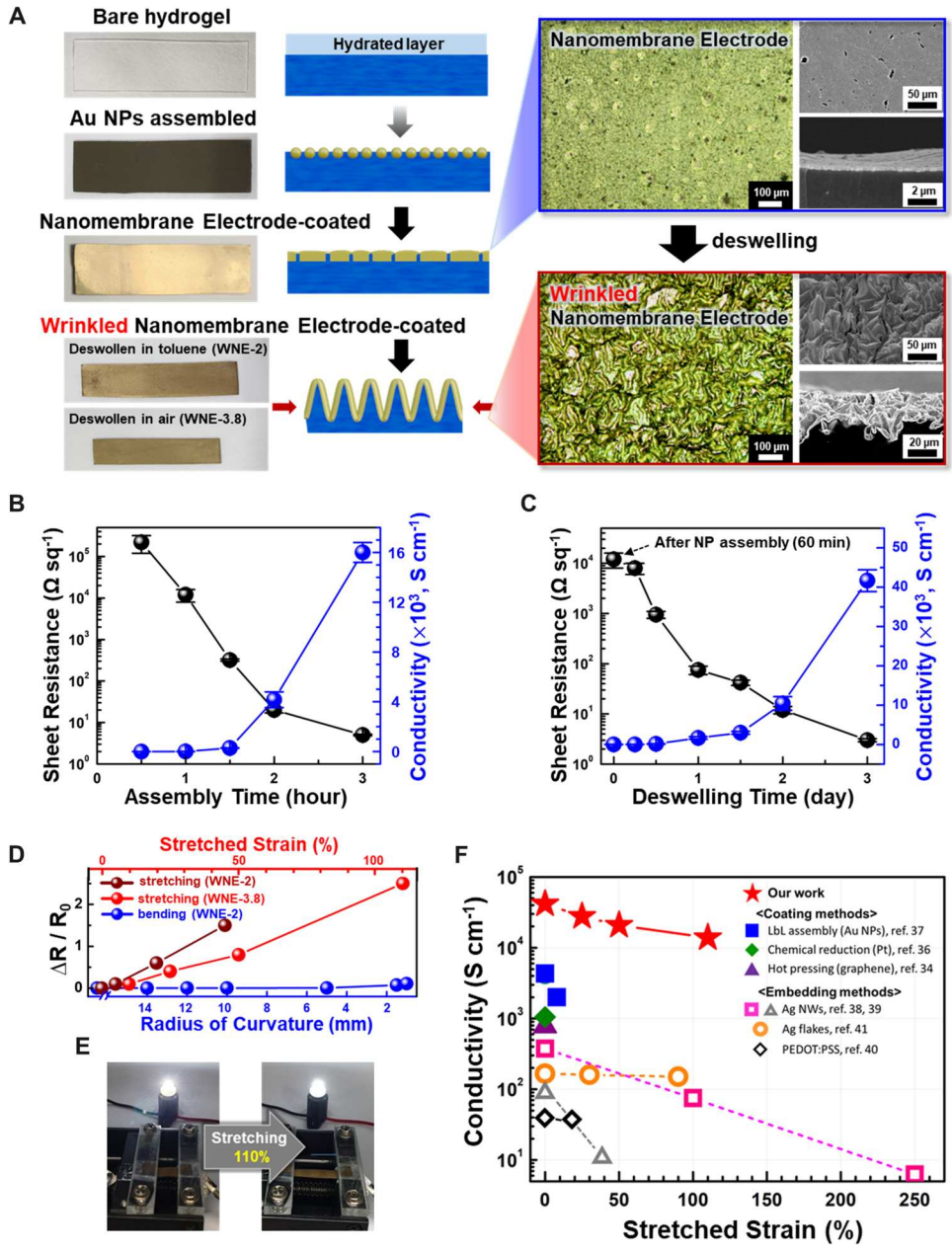

Fig. 2. Preparation of WNE on hydrogel. Photographic images and cross-sectional illustration of the procedure for WNE formation on hydrogel in different stages. (**A**) Optical microscopy and SEM images of the nanomembrane electrode (before deswelling) and WNE (after deswelling). (**B**) Sheet resistance and conductivity of the nanomembrane electrode coated on PAA-*co*-PAAm as a function of assembly time. (**C**) Sheet resistance and conductivity of the WNE coated on PAA-*co*-PAAm as a function of deswelling time after 60 min of NP assembly. Error bars in (B) and (C) represent SD. (**D**) Resistance changes in a WNE coated on PAA-*co*-PAAm (WNE-2 and WNE-3.8) in stretched or bent states as a function of the stretching strain and bending radius. (**E**) Photographic images of WNE-coated PAA-*co*-PAAm connected with light-emitting diodes before and after stretching. (**F**) Electrical conductivity comparison between WNE-coated PAA-*co*-PAAm (our study) and previously reported hydrogel-based electrodes as a function of stretching strain.

These phenomena were further confirmed with a two-phase liquid system based on PEI solution (in water) and TOA-Au NP solution (in toluene) (fig. S8). In this case, the dispersed TOA-Au NPs were gradually transformed to Au nanoplate layers at the water/toluene interface because the surfaces of Au NPs undergoing ligand exchange reactions were changed from hydrophobic (by TOA ligands) to hydrophilic (by PEI), thereby strongly inducing the additional capillary transport of PEI toward the upper TOA-Au NP layer. This capillary transport phenomenon, which was very similar to that observed in our hydrogel system, induced the continuous sintering of Au NPs for the formation of porous Au nanomembrane at the water/toluene interface and further increased their vertical and lateral sizes. Given that previously reported NP assemblies generate monolayers with limited packing densities or

multilayers with high packing density through repetitive deposition steps (*45*, *51*–*56*), our approach using the capillary-assisted in situ NP assembly is advantageous over other approaches reported to date for preparing conductive electrodes on wet hydrogels.

Furthermore, the highly conductive layers (designated as Au nanomembrane electrodes) adsorbed on the hydrogel surface exhibited wrinkled structures through additional deswelling of the hydrogel (Fig. 2A). Although direct and rapid dehydration of the hydrogel in air led to a highly wrinkled structure exhibiting a 3.8-fold increase in surface area (defined as initial surface area of electrode divided by projected surface area of wrinkled electrode), this dehydration process made it difficult to control the deswelling process precisely, which resulted in a nonuniform structure (i.e., WNE-3.8). Therefore, to provide an environmental condition for slow and conformal deswelling, we slowly deswelled the porous Au nanomembrane electrode–coated hydrogel in a nonpolar medium (toluene) according to the dehydration time. In this case, the dehydration process reached a plateau after about 3 days (fig. S9). Consequently, deswelling in a nonpolar medium produced controllable WNEs with porous structures on the hydrogel surfaces, which induced a twofold increase in the surface area (i.e., WNE-2). Because a further deswelling process could result in the excessively increased Young′s modulus and the decreased swelling rate as well as the nonuniform structure, WNE-2 was mainly used for the fabrication of WNE actuators. The strong dependence of the initial swelling ratio of the hydrogel on the solution concentration of infiltrated PEI enabled effective control of the surface areas of the resultant wrinkled electrodes on the hydrogel surfaces (fig. S10).

On the basis of these results, we investigated the electrical properties of nonwrinkled Au nanomembranes (non-WNEs) and wrinkled Au nanomembrane electrode (WNEs) prepared with different processing conditions. When the TOA-Au NPs were deposited onto the hydrogel for 30 min, the TOA-Au NP-assembled hydrogel exhibited an electrical conductivity of 1.7 S cm^{-1} (Fig. 2B). With an increase in the deposition time (assembly time) from 30 to 120 min, the sheet resistance of the nonwrinkled Au nanomembrane decreased sharply from 2.2×10^5 ohms $square^{-1}$ (conductivity, ~1.7 S cm^{-1}) to 5.1 ohms $square^{-1}$ (conductivity, ~1.6×10^4 S cm^{-1}) due to the increased interconnectivity of the Au NPs and subsequent transformation to Au nanoplates on the hydrogel. In addition, the formation of wrinkled structures by deswelling increased the electrical conductivity of the hydrogel electrode. That is, a WNE with a relative surface ratio of 2 (i.e., WNE-2 prepared by TOA-Au NP assembly with a deposition time of 60 min and subsequent deswelling in toluene for 3 days) displayed an electrical conductivity of 4.1×10^4 S cm^{-1} and a sheet resistance of 3 ohms $square^{-1}$ (Fig. 2C), which outperformed those of the previously reported hydrogel-based electrodes. This notable enhancement in electrical properties was mainly attributed to the shortened distance between neighboring Au nanoplates because of additional shrinkage of hydrogel supports. Moreover, the WNE-coated hydrogel exhibited highly stable electrical conductivity under mechanical deformations, including bending and stretching. Specifically, even in the 110% stretched state and fully bent state, the electrical conductivities of the WNE-coated hydrogel were about 1.2×10^4 and 3.5×10^4 S cm^{-1}, respectively (Fig. 2, D and E). In particular, it showed stable electrical stability under repetitive mechanical deformation, maintaining low sheet resistance (< 10 ohms $square^{-1}$) even after 2000 cycles of bending tests. (fig. S11). The WNE-coated hydrogel showed high electrical conductivity and mechanical stretchability at the same time, which outperforms previously reported hydrogel-based electrodes (Fig. 2F).

Electroosmotic performance of the WNE-coated hydrogel

On the basis of these results, we sought to prepare a hydrogel actuator with electroosmotic properties that could reversibly pump the ionic fluid with an applied external electric field (fig. S12). To this end, ionic electrolytes [i.e., 1:1 mixture of aqueous PEI (30 mg/ml) and 1-butyl-3-methylimidazolium tetrafluoroborate ($[BMIM^+][BF_4^-]$)] were infiltrated into WNE-coated hydrogels with a relative surface area of 2 (i.e., WNE-2) that had been prepared by deswelling in toluene phase (Fig. 3A). When an external electric field was applied to the WNE-coated hydrogel, the ionic fluid was induced strongly even at low voltages (<3 V) with a diverse range of frequencies (movie S1). Given that our WNE electrode was prepared by conversion from densely packed Au NPs to Au nanoplates and subsequent deswelling-induced wrinkled structure, a WNE with a large surface area could provide an effective pathway for reversible pumping of ionic fluid. In this case, the amount of the ionic fluid pumped inside the hydrogel was estimated as a function of applied time under constant electric potentials (fig. S13).

The importance of the wrinkled porous structures of electrodes for effective electroosmotic performance is more evidently confirmed in Fig. 3 (B to D). Specifically, in the cases of WNE-1.3 and WNE-2, the amounts of their ionic fluid pumped at 2 V were increased to 7 and 26%, respectively, compared with that of non-WNE (Fig. 3B and fig. S14). On the other hand, when the porosity of WNE was blocked by poly(dimethyl siloxane) (PDMS) coating, the pumped fluid volume decreased by 15% (Fig. 3B). These phenomena were also observed with different electric potentials. That is, when the WNE-coated hydrogel was operated at 1.5, 2, or 3 V, the fluidic volumes were increased by about 18, 26, and 30%, respectively, compared with those of non-WNE–coated hydrogel at the same electric potentials (Fig. 3, C and D). The total and relative amounts of pumped fluids as a function of sample thickness were further examined at a fixed voltage (2 V). In this case, the pumped volumes for three different kinds of samples were almost saturated after 30 s (Fig. 3E), showing a similar relative pumped volume of about 25% regardless of actuator thickness (Fig. 3F). In particular, as shown in Fig. 3F, about 10 to 15% of the ionic fluid was rapidly pumped in a few seconds, which contributed to pumped fluid-induced swelling/deswelling of the hydrogel body. Moreover, we also confirmed that the electroosmotic flow rate of our actuator could be increased to 7.5 μl cm^{-2} s^{-1} V^{-1}, which was more than three times higher than those of conventional electroosmotic devices (<2 μl cm^{-2} s^{-1} V^{-1}), indicating its high electroosmotic performance and efficiency (*57*–*64*). Therefore, the enhanced electroosmotic performance of the WNE-coated hydrogel was mainly caused by the substantial increases in electrode surface area and electrical conductivity due to the wrinkled structure.

Performance of WNE actuators

Upon confirming the noteworthy mechanical, electrical, and electroosmotic properties of WNE-coated hydrogels, we constructed an actuator using the WNE-2–coated hydrogel. We investigated the performance of WNE actuators with an external power supply and an on-board battery (fig. S15). When the WNE actuators were subjected to an electric potential, electroosmotic flow toward

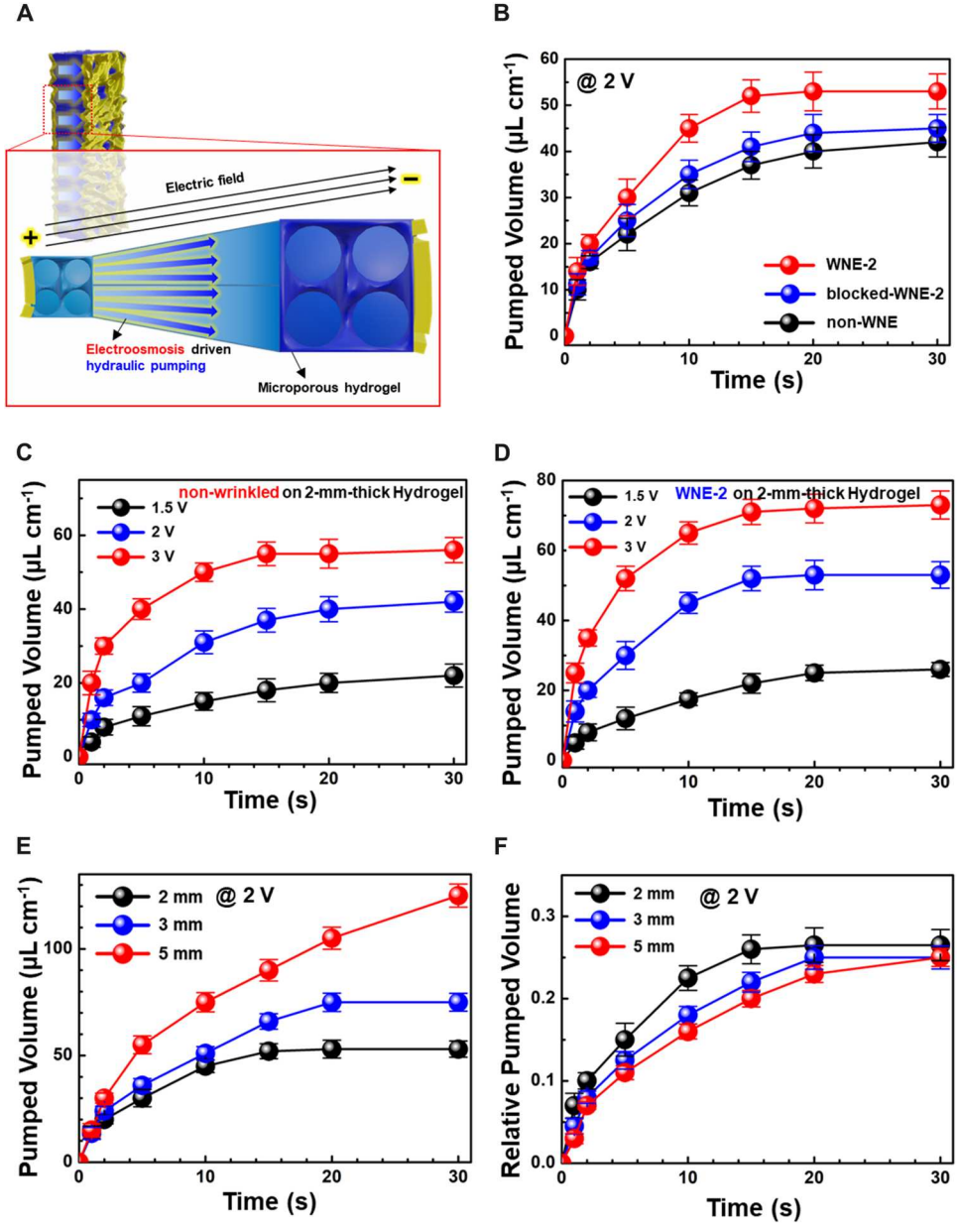

Fig. 3. Electroosmotic performance of WNE-coated hydrogel. (**A**) Schematic illustration of electroosmosis occurring in a WNE-coated hydrogel. (**B**) Electroosmotic pumped volume of non-WNE and WNE-coated PAA-*co*-PAAm (2 mm in thickness) operated at a constant voltage of 2 V. Electroosmotic pumped volume of non-WNE–coated (**C**) and WNE-coated (**D**) PAA-*co*-PAAm (2-mm thick) with different operating voltages. Electroosmotic pumped volume (**E**) and relative pumped volume (**F**) of WNE-2–coated PAA-*co*-PAAm with different thicknesses operating at 2 V. Error bars represent SD.

negative potential was generated, resulting in swelling and deswelling of the hydrogel near the negative and the positive electrodes, respectively (Fig. 4A). These phenomena implied that bending motions of WNE actuators could be easily induced and controlled by the applied electric potential and time (movie S2). In particular, the unique morphologies of electrodes (i.e., wrinkled structure and porosity) in WNE actuators played an important role in achieving high performance of actuators. In contrast, the hydrogel actuators with nonwrinkled electrodes (i.e., non-WNE actuator) and porosity-blocked wrinkled electrodes (i.e., porosity blocked-WNE actuator) showed that their actuation strains were decreased by about 50 and 15 to 25%, respectively, compared with that of WNE actuators (fig. S16). In addition, high electrical conductivity of WNE actuators was also critical for their high actuation performances (fig. S17). Moreover, among various hydrogel bodies with different monomer types and compositions, PAA-*co*-PAAm (8:2) hydrogel exhibited superior actuation performance compared with other hydrogels (fig. S18). On the basis of these results, when an electric potential of 3 V was applied to WNE actuators with thicknesses of 250, 450, and 600 μm, their maximum actuation strains were estimated to be about 43, 45, and 60%, respectively (Fig. 4, B and C). In addition, a considerably short response time (<0.5 s) was observed from

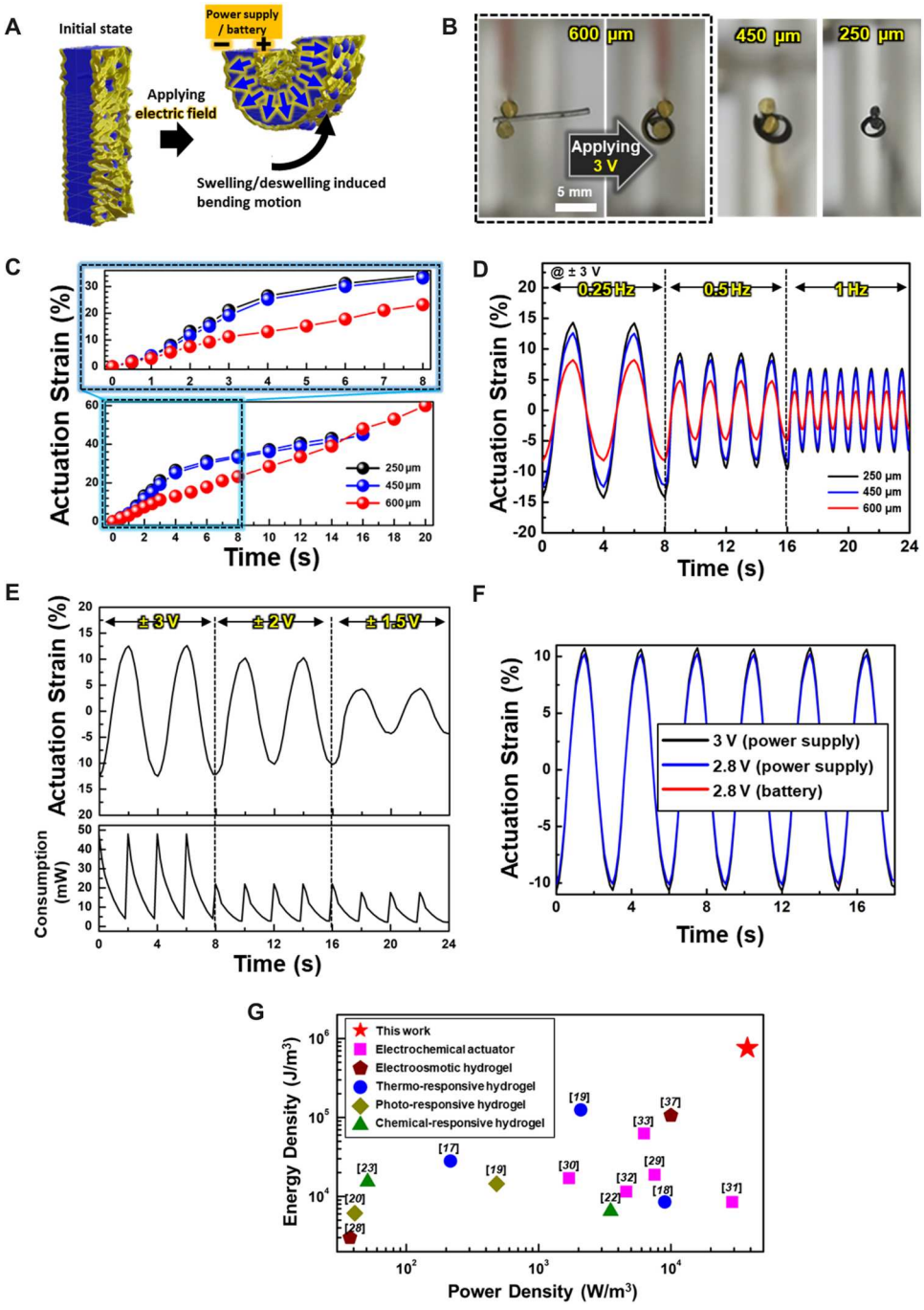

Fig. 4. Performance of WNE actuator. (**A**) Schematic illustration of the WNE actuator showing its working mechanism and operation with a power supply or on-board battery. (**B**) Photographic images of WNE actuators with different thicknesses operating at 3 V. (**C**) Time-dependent actuation strain of WNE actuators with different thicknesses operating at 3 V. (**D**) Actuation strain of WNE actuators with different thicknesses operated at alternating 3 V with different frequencies. (**E**) Actuation strains and power consumption of 450-μm-thick WNE actuators operating at different alternating voltages with a frequency of 0.25 Hz. (**F**) Actuation strains of 450-μm-thick WNE actuators powered by a power supply and battery. (**G**) Performance comparison between WNE actuators and other mechanism-driven hydrogel actuators.

all the actuators except the 600-μm-thick actuator (Fig. 4D). Although the 600-μm-thick actuator exhibited the highest actuation strain among the three different actuators, it exhibited a relatively slow response speed due to its thickness. Therefore, the 450-μm-thick actuator was selected for further investigation and application. On the basis of these results, the 450-μm-thick actuator was operated with different electric potentials at alternating signals (frequency of 0.25 Hz). In this case, high actuation strains of 12.6, 9.8, and 4.2% were observed at 3, 2, and 1.5 V, respectively (Fig. 4E). In particular, the WNE-actuator exhibited high actuation strains with an enhanced maximum transduction efficiency of 22.8% (maximum 60% strain of 600-μm-thick actuator with an average power consumption of 10 mW) compared with previously reported electrochemical actuators that suffered from low actuation strains below 2% with a transduction efficiency of <7.5% (*31*, *32*) and deteriorating actuation strains with increased thickness of devices (fig. S19) (*29*–*33*, *36*). Because of the low operation voltage and power consumption of WNE actuators, they can be sufficiently operated with on-board electronics and a small battery (movie S3). Moreover, the actuation strain of a small battery-powered WNE actuator was consistent with the actuation strain of a WNE actuator operated with an external power source (Fig. 4F). Furthermore, although our WNE actuator could not generate high force similar to that of a turgor cell–structured electroosmotic hydrogel device (>500 N) (*27*), it showed maximum blocking force of more than 20 mN (2 cm by 0.7 cm by 450 μm, 72 mg), which was higher than those previously reported of electrochemical actuators. Such high force could be induced by effective conversion from osmotic pressure to external force with the aid of electroosmotic pumping inside the hydrogel body having increased Young's modulus (fig. S20). This WNE actuator exhibited high energy and power densities of maximum 7.5×10^5 J m^{-3} and 3.8×10^4 W m^{-3} (4.2×10^5 J m^{-3} and 1.1×10^4 W m^{-3} at the frequency of 0.25 Hz), which were 5 to 10 times higher than those of other mechanism-driven hydrogel actuators (Fig. 4G). In particular, a notable feature of the WNE actuator is that its power density is comparable to that of natural skeletal muscle, although it is still inferior to those of electrostatic and electrothermal soft actuators requiring high voltages (about kilovolts)

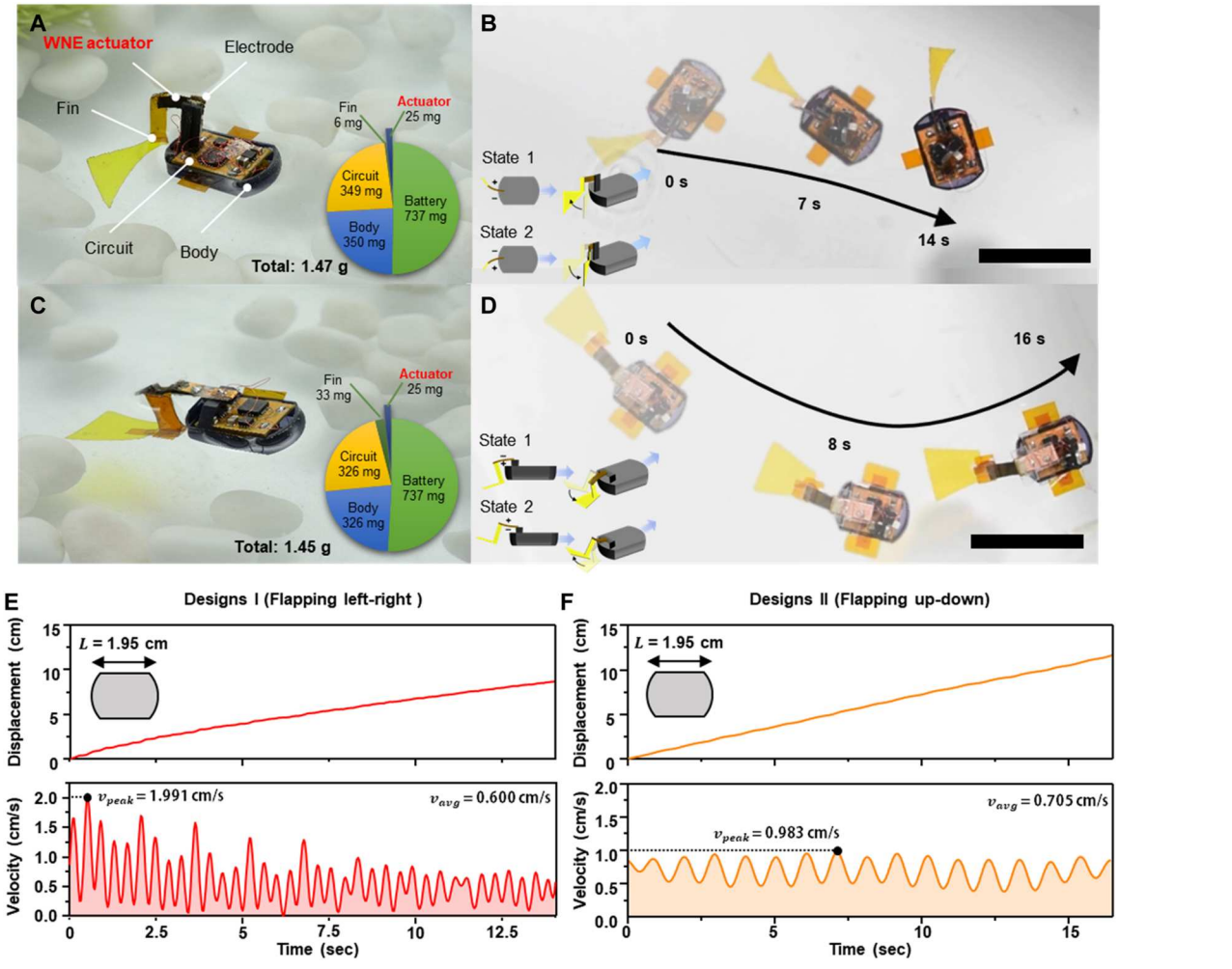

Fig. 5. Demonstration of untethered soft aquabots (flapping motion). (**A**) Photographic image of a soft aquabot with flapping (left-right) motion and a component weight pie chart. (**B**) Photographic image of a moving soft aquabot with a flapping (left-right) motion. Scale bar, 3 cm. (**C**) Photographic image of a soft aquabot with a flapping (up-down) motion and a component weight pie chart. (**D**) Photographic image of a moving soft aquabot with flapping (up-down) motion. Scale bar, 3 cm. Displacement and velocity of flapping aquabots with left-right (**E**) and up-down (**F**) motions operating with a single WNE actuator.

and/or power consumption (>100 mW cm^{-2}) (table S1). These results are notable in that a high-performance WNE actuator with low operation voltage and power consumption can be effectively applied in the development of untethered mobile robots, requiring large strokes of actuators even with small-scale electronic components.

The operation stability and energy/power density of WNE actuators also play an important role in maintaining the actuation performance. To improve the operation stability of our actuator, we encapsulated it with an elastic protective layer to prevent water evaporation. Specifically, imine-incorporated PDMS was uniformly coated on the surface of the WNE actuators by simple dip coating in a solution of bis(3-aminopropyl)–terminated PDMS and benzene-1,3,5-tricarboxaldehyde. Subsequently, a thin (~10 μm) and conformal PDMS layer was formed on the WNE actuator within 30 s (fig. S21). Because of the low thickness and low modulus (~150 kPa) of

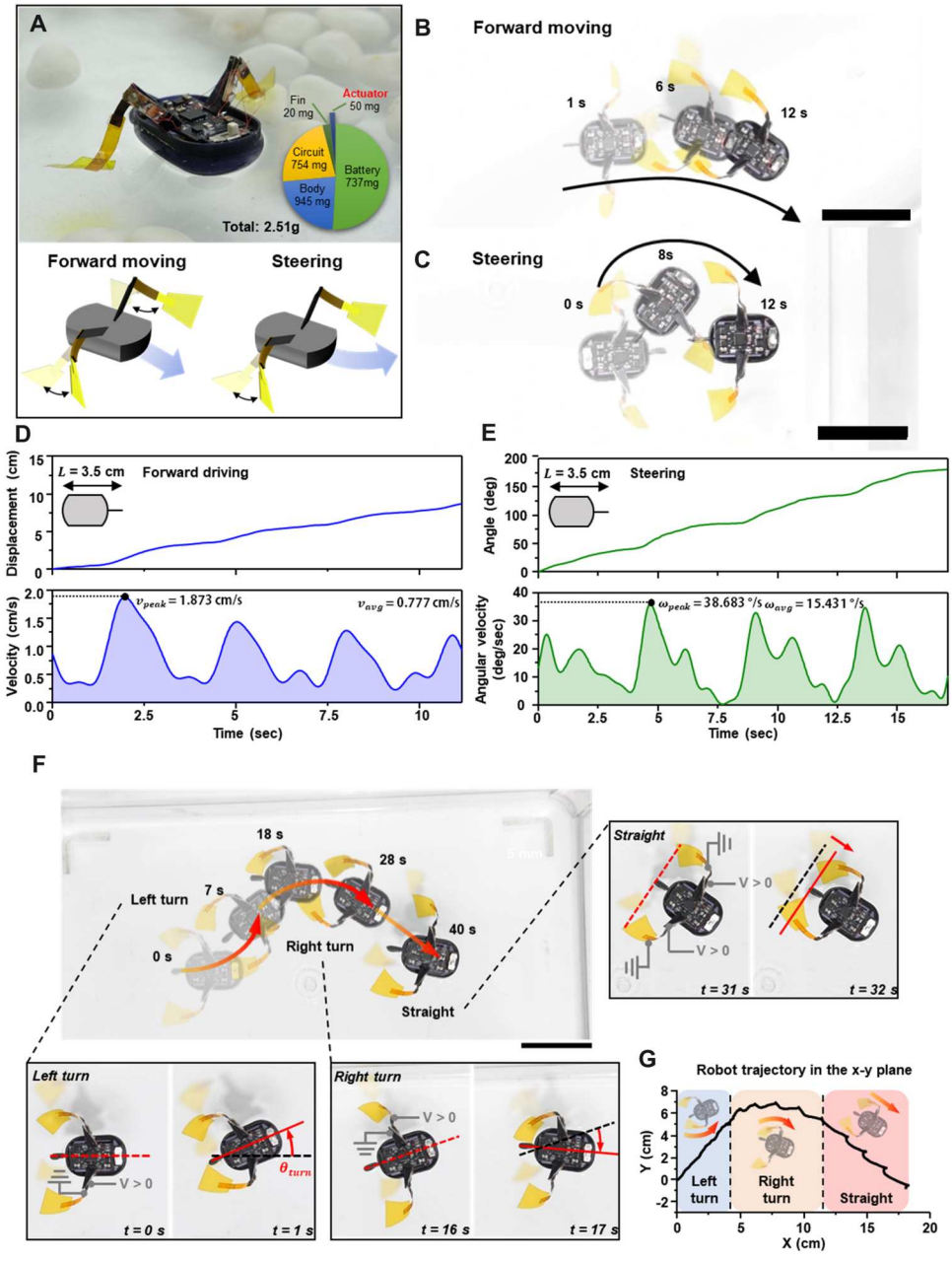

Fig. 6. Demonstration of untethered soft aquabot (sculling motion). (**A**) Photographic and schematic images of a soft aquabot with a sculling motion and a component weight pie chart. Photographic images of forward-moving (**B**) and steering (**C**) soft aquabots with a sculling motion. Scale bar, 3 cm. (**D**) Displacement and velocity of a soft aquabot with a sculling motion. (**E**) Steered angle and angular velocity of a soft aquabot with a sculling motion. (**F**) Photographic images of a turning and forward-moving soft aquabot with sculling motion by feed forward command. Scale bar, 3 cm. In addition to forward swimming, the aquabot allows to make turns by controlling the timing of activation of the two fins. Steering can be performed by applying the fins with different signals independently. (**G**) The tracked swimming trajectory corresponding to the demonstration.

the PDMS-coating layer, the Young's modulus of the PDMS-coated WNE actuator was increased slightly from 4.2 to 4.5 MPa. Although the actuation strain of the PDMS-coated WNE actuator was decreased by about 20% compared with that of a WNE actuator without a PDMS layer due to the increased Young's modulus and blocked porous structures of WNE (fig. S22), PDMS-encapsulated WNE actuators operated stably more than 500 cycles, maintaining more than 90% of the initial actuation strain (fig. S23). Although it is still challenging to realize highly repeatable and precise actuating motions because of the presence of various and complicated parameters affecting the hydrogel swelling, the repeatability and precision of actuation motions shown in the WNE actuator can be further enhanced by the additional coating of encapsulation layer onto the WNE actuator (fig. S24). Moreover, most previously reported hydrogel actuators cannot be operated stably for more than 10 cycles in air, which has been a serious barrier to practical utilization of soft robots.

Untethered soft aquabots by WNE actuators

To further demonstrate the notable characteristics of WNE actuators in application-specific scenarios, we constructed untethered autonomous soft aquabots (i.e., WNE actuator–based aquabots with small microcontrollers and batteries) requiring large strokes of actuators to generate sufficient thrust forces (Fig. 5A and fig. S25). To generate large propulsion in water, we attached 3-cm-long fins with anisotropic shapes to 1.2-cm-long WNE actuators (fig. S26). On the basis of these components, two different types of aquatic robots were prepared, possibly allowing flapping and sculling motions similar to those shown in natural organisms.

First, we fabricated 1.95-cm-sized aquabots with flapping motions (Fig. 5), which included a battery (3.7 V, 30 mA·hour, 737 mg) and printed circuit board (326 mg) (fig. S27). A single WNE actuator (1.2 cm by 0.4 cm by 450 μm, 25 mg) was integrated into three-dimensional (3D)–printed bodies (350 mg for flapping left-right and 326 mg for flapping up-down) embedding the circuit board and battery (Fig. 5, A to D). Unlike previously reported soft aquabots that required relatively lengthy soft actuators to generate sufficient thrust, our soft aquabots can be driven by 1.2-cm-long WNE actuators with attached fins (flapping left-right: 2.5 cm by 1 cm, 6 mg; flapping up-down: 2 cm by 2 cm, 33 mg). When the WNE actuator was subjected to an alternating 2.8-V potential with a frequency of 1 Hz, the up-down or right-left flapping motions drove the aquabots forward with maximum speeds of 1.02 and 0.5 body length (BL) s^{-1}, respectively (Fig. 5, E and F, and movie S4).

Moreover, steering of the aquabot was accomplished with two independently controlled motions of WNE actuators integrated on the left and right sides of the 3D printed body, which generated a sculling motion (Fig. 6). To this end, a 3.5-cm aquabot comprising a battery, circuit board, body (945 mg), two actuators (1.2 cm by 0.4 cm by 450 μm, 25 mg), and fins (20 mg) was additionally fabricated, as shown in Fig. 6A and fig. S27. By changing the input electrical signals (2.8 V, 0.33 Hz) on each side of the actuators, the sculling aquabot produced forward, right-turn, and left-turn motions (Fig. 6, B and C, and movie S4) under untethered conditions. Specifically, the forward movements showed a maximum speed of 0.53 BL s^{-1}, and turning movements showed a maximum angular speed of 38.6° s^{-1} (Fig. 6, D and E). We further demonstrated the controllability of our aquabot by performing a maneuvering test with a feed forward command. By controlling the two actuators with a programed control signal at alternating 2.8-V potential, we demonstrated that the robot can be steered and make forward movements for maneuvering (Fig. 6, F and G; fig. S28; and movie S5). Although WNE actuator–based soft aquabots cannot maximize thrust because of the reverse dragging force during the recovery stroke, we believe that they are one of the smallest soft aquabots among the various aquabots containing on-board electric boards and power sources reported to date (fig. S29 and table S2). As shown in the mass distributions of the robots (Figs. 5, A and C, and 6A), the WNE actuator occupied just 2% of the body mass, but its power density was high enough for propulsion of the aquabots along the water surface. In particular, considering that conventional actuation components such as transmissions, linkages, and gear trains have a notable effect on the mechanical efficiencies of actuation applications, our WNE actuator, which can be operated without such components, can be effectively applied in a small-scale autonomous robot system.

DISCUSSION

We demonstrated low voltage–driven WNE actuators that overcame the drawbacks of prior hydrogel actuators, including slow response time, low power density, and poor controllability. This hydrogel actuator was fabricated via capillary-assisted in situ NP assembly, which provided a facile and effective pathway for formation of a wrinkled nanomembrane layer with a large surface area and a porous structure on the hydrogel surface. The WNE-coated hydrogel exhibited high electrical conductivity and mechanical flexibility at the same time, which far exceeded those of previously reported hydrogel-based electrodes (Fig. 2F). These notable features of the WNE-coated hydrogel resulted in high actuating performance (i.e., strain of >50%, energy density of $>7 \times 10^5$ J m^{-3}, and power density of $>3 \times 10^4$ W m^{-3}) with a low bias voltage of 3 V or less based on efficient electroosmosis pumping inside the hydrogel body. This high performance under low operation voltage is difficult to realize with existing electrically actuating soft actuators, including electrothermal (e.g., liquid crystal elastomer and shape memory alloy), electrochemical (e.g., ionic polymer-metal composite), and electrostatic (e.g., dielectric elastomer and hydraulically amplified self-healing electrostatic) mechanism-driven actuators.

The high performance of WNE actuators was further demonstrated by fabricating untethered soft aquabots that are smaller and faster than state-of-the-art soft aquabots driven by dielectric elastomer actuators, ionic polymer-metal complex actuators, and others (fig. S29 and table S2). In particular, our soft aquabots based on WNE actuators could be constructed without any high-voltage converter and conventional transmission system, which have considerably limited the miniaturization of soft robots. These characteristics of WNE actuators with high power density enabled us to build a small-scale aquabot 2 cm in body size with on-board power. The resulting robot demonstrated maneuvering with two actuators by feedforward control command. However, to be a fully autonomous robotic system, sensing components should be further integrated for the recognition of position and orientation of the robot. We believe that our approach could provide a basis for developing lightweight, high-performance soft actuators and robots at small scale that require a variety of motions under electric stimuli.

MATERIALS AND METHODS

Synthesis of TOA-Au NPs

The Brust method was used for the synthesis of TOA-Au NPs. First, 20 mM TOA bromide (98%; Sigma-Aldrich) was dissolved in toluene (80 ml), and 30 mM gold(III) chloride trihydrate ($HAuCl_4 \cdot 3H_2O$; ≥99.9%; Sigma-Aldrich) was dissolved in deionized water (30 ml). They were mixed for more than 30 min with stirring, and the toluene phase was separated. Then, 0.4 M sodium borohydride ($NaBH_4$; 99.99%; Sigma-Aldrich) dissolved in deionized water (25 ml) was added to the separated toluene phase with stirring. After 3 hours of reduction reaction, the solution of TOA-Au NPs was washed several times with H_2SO_4 (0.1 M), NaOH (0.1 M), and deionized water.

Synthesis of the PAA-co-PAAm hydrogel film

First, acrylic acid (Sigma-Aldrich) and acrylamide (Sigma-Aldrich) were dissolved in deionized water at a molar ratio of 4:1 (12 and 3 mM, respectively). Then, 200 μl of ethylene glycol dimethacrylate (98%; Sigma-Aldrich) and 30 mg of 2,2-dimethoxy-2-phenylacetophenone (99%; Sigma-Aldrich) dissolved in dimethyl sulfoxide (99.9%; Sigma-Aldrich), which served as cross-linker and initiator, respectively, were added to the aqueous solution of acrylic acid and acrylamide. The prepared solution was confined within a polyethylene terephthalate (PET) frame with a specific thickness (50 to 2000 μm) sandwiched between slide glasses. The ultraviolet light was irradiated for 30 min to polymerize the confined solutions.

Preparation of WNE on hydrogel

First, the PAA-*co*-PAAm hydrogels were immersed in aqueous PEI solutions (1 to 30 mg ml^{-1}) for more than 24 hours. Because of infiltration of the PEI into the hydrogel matrix, the hydrogel films were swollen depending on the concentrations of PEI solutions. Then, the swollen PEI-infiltrated hydrogel was dipped into a toluene solution containing TOA-Au NPs. With increasing deposition time of TOA-Au NPs, the adsorbed Au NPs were converted into a porous Au nanomembrane film by capillary-assisted in situ NP assembly. Furthermore, additional deswelling of the Au nanomembrane electrode–coated hydrogel in air (3 hours) or toluene (3 days) led to WNEs having different relative surface ratios as a function of deswelling time.

MD simulations

For the construction of a model system that consists of PEI chains between Au (100) surfaces, all-atom MD simulations were conducted. The *n* PEI chains were positioned between Au slabs [FCC stacked with a (100) face consisting of a 12-by-12 supercell] for the initial model system. The PEI chain is modeled as a randomly branched chain with a molecular weight of 777 g mol^{-1}. On the basis of this system constitution, NPT-ensemble MD simulations were performed at 298 K and 1 bar using Forcite module with COMPASS force field (COMPASS II, implemented in Material Studio package) (*65*). To maintain the temperature (298 K) and pressure (1 bar), we used the Nose-Hoover-Langevin thermostat (*66*) and Parrinello-Rahman barostat (*67*). The Ewald summation method was used to calculate the electrostatic potential energy (accuracy, 0.1 kcal mol^{-1}; buffer width, 0.5 Å). The atom-based technique (cutoff distance, 12.5 Å; spline width, 1 Å) was used to calculate the van der Waals potential energy.

Characterization of WNE-coated hydrogels

For the characterization of WNE-coated hydrogels, samples were first freeze-dried at −80°C for more than 24 hours. Then, the morphology and thickness of WNE-coated hydrogels was characterized and measured using field-emission scanning electron microscopy (FE-SEM; Hitachi s4800). We further confirmed the results by conducting cryo–FE-SEM (Quanta-3D FEG). The sheet resistance of the sample was measured using a two-point probe (Keithley 4200-SCS) and a four-point probe (MCP-T610, Mitsubishi Chemical Analytech).

Measurement of actuator performance

For measurements of actuation performance, platinum-coated poles (2 mm in diameter) or carbon poles (1 mm in diameter) were used to apply electrical potentials to the WNE-hydrogel actuators and minimize mechanical and electrochemical damage during the operation. The bending motions of WNE-hydrogel actuators were recorded by a digital camera (Nikon D750; 30 frames s^{-1}) for different electric potential conditions. The bending strain (ϵ) was estimated as previously defined (*33*, *68*):

$$\epsilon = \frac{\Delta L_1 + \Delta L_2}{L} = \frac{d}{R}$$

$$\left(\frac{R - \frac{d}{2}}{R + \frac{d}{2}} = \frac{L + \Delta L_2}{L + \Delta L_1} \right)$$

where ϵ, *L*, *d*, and *R* are the actuation strain, the actuator length, the thickness of the actuator, and the bending radius of actuator, respectively. Energy density (E_d), power density (P_d) and transduction efficiency (electrical energy to mechanical energy conversion efficiency, $\eta_{transduction}$) of the soft actuator were estimated by the following equations, which have been widely used for elastically actuating materials (*31*–*33*)

$$E_d = \frac{\gamma \cdot \varepsilon^2}{2}$$

$$P_d = \frac{E_d}{t}$$

$$\eta_{transduction}(\%) = \frac{P_{mechanical}}{P_{electricalinput}} = \frac{P_d \cdot Vol}{IV} \times 100\%$$

where γ, ε, and *t* is the Young's modulus of actuators, the actuation strain of the actuators, and the time required for one cycle, respectively.

Fabrication of soft aquabots

Bodies of aquabots were fabricated with a 3D printer (Project MJP 2500, 3D Systems Inc.). Printed circuit boards were prepared by integrating a microcontroller (ATtiny2313A, Microchip Technology), motor driver (C0805C104K5RAC7800, KEMET), regulator (TPS74529PQWDRVRQ1, Texas Instruments), and capacitors (C0805C224K1RAC7800, KEMET). Fins were fabricated by cutting 50-μm-thick polyimide films and physically attached to

the WNE actuator by placing elastic PET films between them. The battery (3.7 V, 30 mA·hour, 737 mg), polychlorinated biphenyl, and fin-attached WNE actuator were integrated into the 3D printed body. The prepared aquabots were floated on water surfaces, and their locomotion was recorded with a digital camera (Nikon D750; 30 frames s^{-1}).

Supplementary Materials

This PDF file includes:
Figs. S1 to S29
Tables S1 and S2
References (*69*–*83*)

Other Supplementary Material for this manuscript includes the following:
Movies S1 to S5

REFERENCES AND NOTES

1. K. Y. Ma, P. Chirarattananon, S. B. Fuller, R. J. Wood, Controlled flight of a biologically inspired, insect-scale robot. *Science* **340**, 603–607 (2013).
2. Y. Chen, H. Zhao, J. Mao, P. Chirarattananon, E. F. Helbling, N. S. P. Hyun, D. R. Clarke, R. J. Wood, Controlled flight of a microrobot powered by soft artificial muscles. *Nature* **575**, 324–329 (2019).
3. Y. Wu, J. K. Yim, J. Liang, Z. Shao, M. Qi, J. Zhong, Z. Luo, X. Yan, M. Zhang, X. Wang, R. S. Fearing, R. J. Full, L. Lin, Insect-scale fast moving and ultrarobust soft robot. *Sci. Robot.* **4**, eaax1594 (2019).
4. Z. Zhakypov, K. Mori, K. Hosoda, J. Paik, Designing minimal and scalable insect-inspired multi-locomotion millirobots. *Nature* **571**, 381–386 (2019).
5. Y. Tang, Y. Chi, J. Sun, T.-H. Huang, O. H. Maghsoudi, A. Spence, J. Zhao, H. Su, J. Yin, Leveraging elastic instabilities for amplified performance: Spine-inspired high-speed and high-force soft robots. *Sci. Adv.* **6**, eaaz6912 (2020).
6. J. Liang, Y. Wu, J. K. Yim, H. Chen, Z. Miao, H. Liu, Y. Liu, Y. Liu, D. Wang, W. Qiu, Z. Shao, M. Zhang, X. Wang, J. Zhong, L. Lin, Electrostatic footpads enable agile insect-scale soft robots with trajectory control. *Sci. Robot.* **6**, eabe7906 (2021).
7. S. I. Rich, R. J. Wood, C. Majidi, Untethered soft robotics. *Nat. Electron.* **1**, 102–112 (2018).
8. C. A. Aubin, S. Choudhury, R. Jerch, L. A. Archer, J. H. Pikul, R. F. Shepherd, Electrolytic vascular systems for energy-dense robots. *Nature* **571**, 51–57 (2019).
9. G. Li, X. Chen, F. Zhou, Y. Liang, Y. Xiao, X. Cao, Z. Zhang, M. Zhang, B. Wu, S. Yin, Y. Xu, H. Fan, Z. Chen, W. Song, W. Yang, B. Pan, J. Hou, W. Zou, S. He, X. Yang, G. Mao, Z. Jia, H. Zhou, T. Li, S. Qu, Z. Xu, Z. Huang, Y. Luo, T. Xie, J. Gu, S. Zhu, W. Yang, Self-powered soft robot in the Mariana Trench. *Nature* **591**, 66–71 (2021).
10. T. Li, G. Li, Y. Liang, T. Cheng, J. Dai, X. Yang, B. Liu, Z. Zeng, Z. Huang, Y. Luo, T. Xie, W. Yang, Fast-moving soft electronic fish. *Sci. Adv.* **3**, e1602045 (2017).
11. C. Christianson, N. N. Goldberg, D. D. Deheyn, S. Cai, M. T. Tolley, Translucent soft robots driven by frameless fluid electrode dielectric elastomer actuators. *Sci. Robot.* **3**, eaat1893 (2018).
12. Z. Chen, S. Shatara, X. Tan, Modeling of biomimetic robotic fish propelled by an ionic polymer–metal composite caudal fin. *IEEE ASME Trans. Mechatron.* **15**, 448–459 (2010).
13. Z. Chen, A review on robotic fish enabled by ionic polymer–metal composite artificial muscles. *Robotics Biomim.* **4**, 24 (2017).
14. R. Khodambashi, S. Berman, X. He, D. M. Aukes, Miniaturized untethered soft robots using hydrogel-based soft voxel actuators, in *2021 IEEE 4th International Conference on Soft Robotics (RoboSoft)* (IEEE, 2021), pp. 571–574.
15. J. Shu, D. A. Ge, E. Wang, H. Ren, T. Cole, S. Y. Tang, X. Li, X. Zhou, R. Li, H. Jin, W. Li, M. D. Dickey, S. Zhang, A liquid metal artificial muscle. *Adv. Mater.* **33**, 2103062 (2021).
16. H. Zhao, Y. Huang, F. Lv, L. Liu, Q. Gu, S. Wang, Biomimetic 4D-printed breathing hydrogel actuators by nanothylakoid and thermoresponsive polymer networks. *Adv. Funct. Mater.* , 2105544 (2021).
17. R. Khodambashi, Y. Alsaid, R. Rico, H. Marvi, M. M. Peet, R. E. Fisher, S. Berman, X. He, D. M. Aukes, Heterogeneous hydrogel structures with spatiotemporal reconfigurability using addressable and tunable voxels. *Adv. Mater.* **33**, 2005906 (2021).
18. J. Kim, A. Hanna James, M. Byun, D. Santangelo Christian, C. Hayward Ryan, Designing responsive buckled surfaces by halftone gel lithography. *Science* **335**, 1201–1205 (2012).
19. Y. Zhao, C.-Y. Lo, L. Ruan, C.-H. Pi, C. Kim, Y. Alsaid, I. Frenkel, R. Rico, T.-C. Tsao, X. He, Somatosensory actuator based on stretchable conductive photothermally responsive hydrogel. *Sci. Robot.* **6**, eabd5483 (2021).
20. G. Li, G. Fan, Z. Liu, Z. Liu, J. Jiang, Y. Zhao, Photoresponsive shape memory hydrogels for complex deformation and solvent-driven actuation. *ACS Appl. Mater. Interfaces* **12**, 6407–6418 (2020).
21. X. Qian, Y. Zhao, Y. Alsaid, X. Wang, M. Hua, T. Galy, H. Gopalakrishna, Y. Yang, J. Cui, N. Liu, M. Marszewski, L. Pilon, H. Jiang, X. He, Artificial phototropism for omnidirectional tracking and harvesting of light. *Nat. Nanotechnol.* **14**, 1048–1055 (2019).
22. L. Huang, R. Jiang, J. Wu, J. Song, H. Bai, B. Li, Q. Zhao, T. Xie, Ultrafast digital printing toward 4D shape changing materials. *Adv. Mater.* **29**, 1605390 (2017).
23. Y. Ma, M. Hua, S. Wu, Y. Du, X. Pei, X. Zhu, F. Zhou, X. He, Bioinspired high-power-density strong contractile hydrogel by programmable elastic recoil. *Sci. Adv.* **6**, eabd2520 (2020).
24. C. Ma, X. le, X. Tang, J. He, P. Xiao, J. Zheng, H. Xiao, W. Lu, J. Zhang, Y. Huang, T. Chen, A multiresponsive anisotropic hydrogel with macroscopic 3D complex deformations. *Adv. Funct. Mater.* **26**, 8670–8676 (2016).
25. M. Ji, N. Jiang, J. Chang, J. Sun, Near-infrared light-driven, highly efficient bilayer actuators based on polydopamine-modified reduced graphene oxide. *Adv. Funct. Mater.* **24**, 5412–5419 (2014).
26. D. Lunni, M. Cianchetti, C. Filippeschi, E. Sinibaldi, B. Mazzolai, Plant-inspired soft bistable structures based on hygroscopic electrospun nanofibers. *Adv. Mater. Interfaces* **7**, 1901310 (2020).
27. H. Na, Y. W. Kang, C. S. Park, S. Jung, H. Y. Kim, J. Y. Sun, Hydrogel-based strong and fast actuators by electroosmotic turgor pressure. *Science* **376**, 301–307 (2022).
28. C. Y. Li, S. Y. Zheng, X. P. Hao, W. Hong, Q. Zheng, Z. L. Wu, Spontaneous and rapid electro-actuated snapping of constrained polyelectrolyte hydrogels. *Sci. Adv.* **8**, eabm9608 (2022).
29. L. Liu, C. Wang, Z. Wu, Y. Xing, Ultralow-voltage-drivable artificial muscles based on a 3D structure MXene-PEDOT:PSS/AgNWs electrode. *ACS Appl. Mater. Interfaces* **14**, 18150–18158 (2022).
30. M. Kotal, R. Tabassian, S. Roy, S. Oh, I.-K. Oh, Metal–organic framework-derived graphitic nanoribbons anchored on graphene for electroionic artificial muscles. *Adv. Funct. Mater.* **30**, 1910326 (2020).
31. G. Wu, X. Wu, Y. Xu, H. Cheng, J. Meng, Q. Yu, X. Shi, K. Zhang, W. Chen, S. Chen, High-performance hierarchical black-phosphorous-based soft electrochemical actuators in bioinspired applications. *Adv. Mater.* **31**, 1806492 (2019).
32. C. Lu, Y. Yang, J. Wang, R. Fu, X. Zhao, L. Zhao, Y. Ming, Y. Hu, H. Lin, X. Tao, Y. Li, W. Chen, High-performance graphdiyne-based electrochemical actuators. *Nat. Commun.* **9**, 752 (2018).
33. S. Umrao, R. Tabassian, J. Kim, V. H. Nguyen, Q. Zhou, S. Nam, I.-K. Oh, MXene artificial muscles based on ionically cross-linked $Ti_3C_2T_x$ electrode for kinetic soft robotics. *Sci. Robot.* **4**, eaaw7797 (2019).
34. M. Kotal, J. Kim, R. Tabassian, S. Roy, V. H. Nguyen, N. Koratkar, I. K. Oh, Highly bendable ionic soft actuator based on nitrogen-enriched 3D hetero-nanostructure electrode. *Adv. Funct. Mater.* **28**, 1802464 (2018).
35. Y. Yan, T. Santaniello, L. G. Bettini, C. Minnai, A. Bellacicca, R. Porotti, I. Denti, G. Faraone, M. Merlini, C. Lenardi, P. Milani, Electroactive ionic soft actuators with monolithically integrated gold nanocomposite electrodes. *Adv. Mater.* **29**, 1606109 (2017).
36. H. S. Wang, J. Cho, D. S. Song, J. H. Jang, J. Y. Jho, J. H. Park, High-performance electroactive polymer actuators based on ultrathick ionic polymer–metal composites with nanodispersed metal electrodes. *ACS Appl. Mater. Interfaces* **9**, 21998–22005 (2017).
37. J. Ko, D. Kim, Y. Song, S. Lee, M. Kwon, S. Han, D. Kang, Y. Kim, J. Huh, J. S. Koh, J. Cho, Electroosmosis-driven hydrogel actuators using hydrophobic/hydrophilic layer-by-layer assembly-induced crack electrodes. *ACS Nano* **14**, 11906–11918 (2020).
38. Q. Zhou, J. Lyu, G. Wang, M. Robertson, Z. Qiang, B. Sun, C. Ye, M. Zhu, Mechanically strong and multifunctional hybrid hydrogels with ultrahigh electrical conductivity. *Adv. Funct. Mater.* **31**, 2104536 (2021).
39. C. Lim, Y. Shin, J. Jung, J. H. Kim, S. Lee, D. H. Kim, Stretchable conductive nanocomposite based on alginate hydrogel and silver nanowires for wearable electronics. *APL Materials* **7**, 031502 (2019).
40. B. Lu, H. Yuk, S. Lin, N. Jian, K. Qu, J. Xu, X. Zhao, Pure PEDOT:PSS hydrogels. *Nat. Commun.* **10**, 1043 (2019).
41. Y. Ohm, C. Pan, M. J. Ford, X. Huang, J. Liao, C. Majidi, An electrically conductive silver–polyacrylamide–alginate hydrogel composite for soft electronics. *Nat. Electron.* **4**, 185–192 (2021).
42. Y. Wang, S. Gong, D. Gómez, Y. Ling, L. W. Yap, G. P. Simon, W. Cheng, Unconventional janus properties of enokitake-like gold nanowire films. *ACS Nano* **12**, 8717–8722 (2018).
43. S. Liu, D. S. Shah, R. Kramer-Bottiglio, Highly stretchable multilayer electronic circuits using biphasic gallium-indium. *Nat. Mater.* **20**, 851–858 (2021).

44. N. Matsuhisa, D. Inoue, P. Zalar, H. Jin, Y. Matsuba, A. Itoh, T. Yokota, D. Hashizume, T. Someya, Printable elastic conductors by in situ formation of silver nanoparticles from silver flakes. *Nat. Mater.* **16**, 834–840 (2017).
45. D. Jung, C. Lim, H. J. Shim, Y. Kim, C. Park, J. Jung, S. I. Han, S. H. Sunwoo, K. W. Cho, G. D. Cha, D. C. Kim, J. H. Koo, J. H. Kim, T. Hyeon, D. H. Kim, Highly conductive and elastic nanomembrane for skin electronics. *Science* **373**, 1022–1026 (2021).
46. D. Han, C. Farino, C. Yang, T. Scott, D. Browe, W. Choi, J. W. Freeman, H. Lee, Soft robotic manipulation and locomotion with a 3D-printed electroactive hydrogel. *ACS Appl. Mater. Interfaces* **10**, 17512–17518 (2018).
47. Y. Shin, M.-Y. Choi, J. Choi, J.-H. Na, S. Y. Kim, Design of an electro-stimulated hydrogel actuator system with fast flexible folding deformation under a low electric field. *ACS Appl. Mater. Interfaces* **13**, 15633–15646 (2021).
48. S. Kang, D. Nam, J. Choi, J. Ko, D. Kim, C. H. Kwon, J. Huh, J. Cho, Highly conductive paper/textile electrodes using ligand exchange reaction-induced in situ metallic fusion. *ACS Appl. Mater. Interfaces* **11**, 12032–12042 (2019).
49. Y. Ko, M. Kwon, W. K. Bae, B. Lee, S. W. Lee, J. Cho, Flexible supercapacitor electrodes based on real metal-like cellulose papers. *Nat. Commun.* **8**, 536 (2017).
50. J. N. Israelachvili, in *Intermolecular and Surface Forces (Third Edition)*, J. N. Israelachvili, Ed. (Academic Press, 2011), pp. 253–289.
51. M. Matsukawa, K.-H. Wang, Y. Imura, T. Kawai, Au nanoparticle monolayer nanosheets as flexible transparent conductive electrodes. *ACS Appl. Nano Mater.* **4**, 10845–10851 (2021).
52. S. Shi, T. P. Russell, Nanoparticle assembly at liquid–liquid interfaces: From the nanoscale to mesoscale. *Adv. Mater.* **30**, 1800714 (2018).
53. C. Xing, S. Zhong, D. Liu, T. Zhang, A. Cao, P. Zeng, D. Men, C. Li, W. Cai, Y. Li, Hydrogel film@Au nanoparticle arrays based on self-assembly co-assisted by electrostatic attraction and hydrogel-shrinkage for SERS detection with active gaps. *Adv. Mater. Interfaces* **8**, 2101055 (2021).
54. M. U. B. Christiansen, N. Seselj, C. Engelbrekt, M. Wagner, F. N. Stappen, J. Zhang, Chemically controlled interfacial nanoparticle assembly into nanoporous gold films for electrochemical applications. *J. Mater. Chem. A* **6**, 556–564 (2018).
55. Z. Ye, C. Li, Q. Chen, Y. Xu, S. E. J. Bell, Self-assembly of colloidal nanoparticles into 2D arrays at water-oil interfaces: Rational construction of stable SERS substrates with accessible enhancing surfaces and tailored plasmonic response. *Nanoscale* **13**, 5937–5953 (2021).
56. T. Nishimura, N. Ito, K. Kinoshita, M. Matsukawa, Y. Imura, T. Kawai, Fabrication of flexible and transparent conductive nanosheets by the UV-irradiation of gold nanoparticle monolayers. *Small* **16**, 1903365 (2020).
57. R. Kumar, K. Jahan, R. K. Nagarale, A. Sharma, Nongassing long-lasting electro-osmotic pump with polyaniline-wrapped aminated graphene electrodes. *ACS Appl. Mater. Interfaces* **7**, 593–601 (2015).
58. Y. Zhang, M. Tian, L. Wang, H. Zhao, L. Qu, Flexible janus textile-based electroosmotic pump for large-area unidirectional positive water transport. *Adv. Mater. Interfaces* **7**, 1902133 (2020).
59. S. Kusama, K. Sato, S. Yoshida, M. Nishizawa, Self-moisturizing smart contact lens employing electroosmosis. *Adv. Mater. Technol.* **5**, 1900889 (2020).
60. L. Li, X. Wang, Q. Pu, S. Liu, Advancement of electroosmotic pump in microflow analysis: A review. *Anal. Chim. Acta* **1060**, 1–16 (2019).
61. W. Shin, J. M. Lee, R. K. Nagarale, S. J. Shin, A. Heller, A miniature, nongassing electroosmotic pump operating at 0.5 V. *J. Am. Chem. Soc.* **133**, 2374–2377 (2011).
62. S. Sreenath, R. Suman, K. V. Sayana, P. S. Nayanthara, N. G. Borle, V. Verma, R. K. Nagarale, Low-voltage nongassing electroosmotic pump and infusion device with polyoxometalate-encapsulated carbon nanotubes. *Langmuir* **37**, 1563–1570 (2021).
63. X. Wang, C. Cheng, S. Wang, S. Liu, Electroosmotic pumps and their applications in microfluidic systems. *Microfluid. Nanofluidics* **6**, 145–162 (2009).
64. S. K. Vajandar, D. Xu, D. A. Markov, J. P. Wikswo, W. Hofmeister, D. Li, SiO_2-coated porous anodic alumina membranes for high flow rate electroosmotic pumping. *Nanotechnology* **18**, 275705 (2007).
65. H. Sun, COMPASS: An ab initio force-field optimized for condensed-phase applications overview with details on alkane and benzene compounds. *J. Phys. Chem. B.* **102**, 7338–7364 (1998).
66. A. A. Samoletov, C. P. Dettmann, M. A. J. Chaplain, Thermostats for "slow" configurational modes. *J. Stat. Phys.* **128**, 1321–1336 (2007).
67. M. Parrinello, A. Rahman, Polymorphic transitions in single crystals: A new molecular dynamics method. *J. Appl. Phys.* **52**, 7182–7190 (1981).
68. I. Takeuchi, K. Asaka, K. Kiyohara, T. Sugino, N. Terasawa, K. Mukai, T. Fukushima, T. Aida, Electromechanical behavior of fully plastic actuators based on bucky gel containing various internal ionic liquids. *Electrochim. Acta* **54**, 1762–1768 (2009).
69. J. D. W. Madden, N. A. Vandesteeg, P. A. Anquetil, P. G. A. Madden, A. Takshi, R. Z. Pytel, S. R. Lafontaine, P. A. Wieringa, I. W. Hunter, Artificial muscle technology: Physical principles and naval prospects. *IEEE J. Ocean. Eng.* **29**, 706–728 (2004).
70. J. Kwon, S. J. Yoon, Y.-L. Park, Flat inflatable artificial muscles with large stroke and adjustable force-length relations. *IEEE Trans. Robot.* **36**, 743–756 (2020).
71. X. Yang, L. Chang, N. O. Pérez-Arancibia, An 88-milligram insect-scale autonomous crawling robot driven by a catalytic artificial muscle. *Sci. Robot.* **5**, eaba0015 (2020).
72. M. Duduta, E. Hajiesmaili, H. Zhao, R. J. Wood, D. R. Clarke, Realizing the potential of dielectric elastomer artificial muscles. *Proc. Natl. Acad. Sci. U.S.A.* **116**, 2476–2481 (2019).
73. S. Wang, B. Huang, D. McCoul, M. Li, L. Mu, J. Zhao, A soft breaststroke-inspired swimming robot actuated by dielectric elastomers. *Smart Mater. Struct.* **28**, 045006 (2019).
74. J. Shintake, V. Cacucciolo, H. Shea, D. Floreano, Soft biomimetic fish robot made of dielectric elastomer actuators. *Soft Robot.* **5**, 466–474 (2018).
75. Q. Shen, T. Wang, J. Liang, L. Wen, Hydrodynamic performance of a biomimetic robotic swimmer actuated by ionic polymer–metal composite. *Smart Mater. Struct.* **22**, 075035 (2013).
76. D. Bartlett Michael, N. Kazem, M. J. Powell-Palm, X. Huang, W. Sun, J. A. Malen, C. Majidi, High thermal conductivity in soft elastomers with elongated liquid metal inclusions. *Proc. Natl. Acad. Sci. U.S.A.* **114**, 2143–2148 (2017).
77. Q. Zhao, S. Liu, J. Chen, G. He, J. Di, L. Zhao, T. Su, M. Zhang, Z. Hou, Fast-moving piezoelectric micro-robotic fish with double caudal fins. *Robot. Auton. Syst.* **140**, 103733 (2021).
78. L. Wen, Z. Ren, V. di Santo, K. Hu, T. Yuan, T. Wang, G. V. Lauder, Understanding fish linear acceleration using an undulatory biorobotic model with soft fluidic elastomer actuated morphing median fins. *Soft Robot.* **5**, 375–388 (2018).
79. Z. Ye, P. Hou, Z. Chen, I. Member, 2D maneuverable robotic fish propelled by multiple ionic polymer–metal composite artificial fins. *Int. J. Intell. Robot. Appl.* **1**, 195–208 (2017).
80. Z. Chen, T. I. Um, H. B.-Smith, Bio-inspired robotic manta ray powered by ionic polymer–metal composite artificial muscles. *Int. J. Smart Nano Mater.* **3**, 296–308 (2012).
81. S.-H. Song, M. S. Kim, H. Rodrigue, J. Y. Lee, J. E. Shim, M. C. Kim, W. S. Chu, S. H. Ahn, Turtle mimetic soft robot with two swimming gaits. *Bioinspir. Biomim.* **11**, 036010 (2016).
82. A. J. Clark, X. Tan, P. K. McKinley, Evolutionary multiobjective design of a flexible caudal fin for robotic fish. *Bioinspir. Biomim.* **10**, 065006 (2015).
83. R. K. Katzschmann, J. DelPreto, R. MacCurdy, D. Rus, Exploration of underwater life with an acoustically controlled soft robotic fish. *Sci. Robot.* **3**, eaar3449 (2018).

Acknowledgments

Funding: This work was supported by the National Research Foundation of Korea (NRF) grant funded by the Korean government (MSIT; Ministry of Science and ICT) (NRF-2021R1A2C3004151 and NRF-2021R1C1C1011872) and the new faculty research fund of Ajou University and the Ajou University research fund. **Author contributions:** J.K., J.-S.K., and J.C. conceived the idea and interpreted the results. J.K., C.K., D.K., Y.S., S.L., B.Y., S.H., D.K., J.-S.K., and J.C. designed and performed the experiments. J.H. conducted theoretical calculation and simulation. J.K., J.-S.K., and J.C. wrote and revised the manuscript. All authors discussed the results and commented on the manuscript. **Competing interests:** The authors declare that they have no competing interests. **Data and materials availability:** All the data necessary to evaluate the conclusions of the paper are presented in the main text and the Supplementary Materials.

Submitted 21 February 2022
Accepted 19 September 2022
Published 26 October 2022
10.1126/scirobotics.abo6463

Science Robotics

High-performance electrified hydrogel actuators based on wrinkled nanomembrane electrodes for untethered insect-scale soft aquabots

Jongkuk Ko, Changhwan Kim, Dongjin Kim, Yongkwon Song, Seokmin Lee, Bongjun Yeom, June Huh, Seungyong Han, Daeshik Kang, Je-Sung Koh, and Jinhan Cho

Sci. Robot. **7** (71), eabo6463. DOI: 10.1126/scirobotics.abo6463

Science Robotics (ISSN 2470-9476) is published by the American Association for the Advancement of Science. 1200 New York Avenue NW, Washington, DC 20005. The title *Science Robotics* is a registered trademark of AAAS.